

Design of magnonic waveguides using surface anisotropy-induced Bragg mirrors

Grzegorz Centała¹ and Jarosław W. Kłos¹

Institute of Spintronics and Quantum Information, Faculty of Physics and Astronomy, Adam Mickiewicz University, Uniwersytetu Poznańskiego 2, 61-614 Poznań, Poland

(*Electronic mail: grcen@amu.edu.pl)

(Dated: 3 February 2026)

Waveguides are fundamental components for signal transmission in integrated wave-based processing systems. In this paper, we address the challenges in designing magnonic waveguides, including limitations such as non-uniform demagnetizing fields, reduced group velocity, and restricted operating frequency ranges. We propose a magnonic waveguide design with promising properties that overcome these limitations to a significant extent. Specifically, we investigate a waveguide formed within a uniform ferromagnetic layer ($\text{Co}_{20}\text{Fe}_{60}\text{B}_{20}$) by applying surface anisotropy in strip regions, thereby creating Bragg mirror structures to confine spin waves and guide them along a single direction. The proposed waveguide enables the propagation of high-frequency spin waves with high velocities in the ferromagnetic layer while minimizing static demagnetizing effects. We developed a model that allows for spin-wave confinement and guidance in two perpendicular directions by spatially modulating the surface anisotropy. The theoretical model was solved using the finite element method to calculate the dispersion relations of the waveguide modes and analyze their spatial profiles. Additionally, we determine the group velocity and localization characteristics, providing a comprehensive understanding of the waveguide's performance.

Magnonics uses spin waves to process signals at gigahertz frequencies in nanoscale reconfigurable systems and is attractive compared to other wave-based computing technologies¹, such as photonics or phononics, where nanoscale integration and reconfigurability are more challenging^{2–4}. In magnonic systems^{5,6}, information is transmitted between functional blocks by waveguides, as in other wave-processing platforms.

Conventional magnonic waveguides are usually in the form of flat wires^{7–11} – see Fig. 1(a). However, their transmission properties are determined not only by geometry and material selection but also by the configuration of magnetization. In the absence of magnetocrystalline anisotropy and the lack of external magnetic fields, the shape anisotropy forces static magnetization to be oriented along the waveguide axis. In this configuration, the group velocity of the spin wave is significantly reduced⁸. By applying the strong field, one can align the magnetization perpendicularly to the axis of the wire, which increases the group velocity; however, this simultaneously generates wells of static demagnetization field near the edges of the waveguide and induces so-called edge modes^{10,11}.

Another technique to create a waveguide is the spatial modification of the material composition¹², which is also used to fabricate planar one-dimensional magnonic crystals^{13,14}. If the saturation magnetization M_s is lower in the waveguide region – see Fig. 1(b), then we can confine and guide the spin waves of frequencies lower than the ferromagnetic resonance (FMR) frequency of the layer in which the waveguide is embedded can be confined.

The most significant disadvantages of conventional waveguides, therefore, include: (i) limited reconfigurability – the geometry of the waveguide is fixed in the fabrication process, and changing its magnetic configuration must be done by applying a strong external magnetic field – which is technically difficult, (ii) the occurrence of strong static demagnetizing field (when the field is applied perpendicularly to the waveguide) or propagation speed limitation (when the field is

applied along to the waveguide). A way to overcome these problems is to use a homogeneous layer as a conductor for spin waves with induced waveguide(s).

Magnetic waveguides can be spontaneously formed in a uniform layer as magnetic domains^{15–17} or domain walls^{18,19} or imprinted by the temperature gradient²⁰, inhomogeneous Oersted field²¹, inhomogeneous demagnetizing field²². One promising technique involves locally modifying the surface anisotropy to create magnonic waveguides within a uniform ferromagnetic layer – see Fig. 1(c). In such a system, the spin waves of lower frequencies can be guided within trenches of the effective magnetic field landscape shaped by the modification of the surface anisotropy^{23,24}. This approach was also used to design various magnonic systems: magnonic crystals^{25,26}, tunnel junctions²⁷, circulators²⁸.

However, these solutions where the waveguide is imprinted in a ferromagnetic layer [Fig. 1(b,c)] allow for confinement and guidance of the spin waves only in a small range of frequencies limited up to the FMR frequency of the pristine layer.

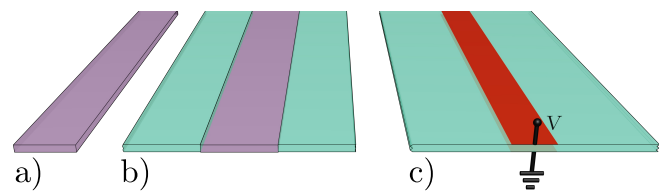


FIG. 1. Selected designs of planar magnonic waveguides: (a) Geometric confinement: a strip of ferromagnetic material (violet) embedded in a nonmagnetic matrix. (b) Material parameter modification: a waveguide formed in the central region of a ferromagnetic layer by reducing the saturation magnetization (violet strip) compared to the surrounding ferromagnet (green areas). (c) Voltage-controlled surface anisotropy: a waveguide induced by locally modified anisotropy (red region on the surface).

Also, the strength of this confinement, i.e. the rate of exponential decay of the spin wave outside the waveguide, depends on the contrast of material parameters (saturation magnetization M_s or surface anisotropy constant K_s) and decreases to zero as the operating frequency approaches the FMR frequency of the uniform layer.

To overcome these limitations and realize the waveguide functionality for higher frequencies, we consider a pair of semi-infinite 1D magnonic crystals (acting as Bragg mirrors²⁹) to confine the spin waves in a linear defect^{30,31} – see Fig. 2(a). In the proposed system, spin waves can be confined in several frequency ranges, corresponding to the successive frequency gaps of the magnonic crystals. In our approach, the magnonic crystals will be created by applying surface anisotropy while preserving the uniformity of the magnetic layer²⁵. We will show that by appropriately playing with choosing the size of the structure, we can obtain both strong confinement of spin waves and a relatively high speed of their propagation along the waveguide.

We used the Landau-Lifshitz equation to describe the magnetization dynamics in the considered system:

$$\frac{d\mathbf{M}}{dt} = -\gamma\mu_0 \left(\mathbf{M} \times \mathbf{H}_{\text{eff}} + \frac{\alpha}{M_s} \mathbf{M} \times (\mathbf{M} \times \mathbf{H}_{\text{eff}}) \right), \quad (1)$$

where $\mathbf{M}(\mathbf{r}, t)$ is magnetization, γ is gyromagnetic ratio, μ_0 is vacuum permeability, α is damping constant, and $\mathbf{H}_{\text{eff}}(\mathbf{r}, t)$ is effective field. Damping is neglected for the considered low-damping material.

For the in-plane applied field, the sample is magnetically saturated. As a result, we can easily linearize Eq. 1 by taking $\mathbf{M}(\mathbf{r}, t) = M_s \hat{\mathbf{x}}_M + \mathbf{m}(\mathbf{r}) e^{i\omega t}$, where the static component is oriented along $\hat{\mathbf{x}}_M$ direction and dynamic component oscillates harmonically in time³².

The effective magnetic field $\mathbf{H}_{\text{eff}}(\mathbf{r}, t)$ consists of the external field of $H_0 \hat{\mathbf{x}}$, the exchange field of $\mathbf{H}_{\text{ex}}(\mathbf{r}, t) = (2A/\mu_0 M_s^2) \Delta \mathbf{M}(\mathbf{r}, t)$, and the dipolar field of $\mathbf{H}_{\text{d}}(\mathbf{r}, t) = -\nabla\varphi(\mathbf{r}, t)$. The symbols A and M_s stand for exchange stiffness constant and saturation magnetization, respectively. The magnetostatic potential (φ) is determined using the Gauss law for magnetism, under the magnetostatic approximation $\Delta\varphi = \nabla \cdot \mathbf{m}$ ³³.

Uniaxial surface anisotropy is introduced by boundary conditions. We took a general form for the boundary conditions for spin waves in the presence of uniaxial out-of-plane anisotropy^{14,32,34}:

$$\hat{\mathbf{x}}_M \times \frac{\partial \mathbf{m}}{\partial \hat{\mathbf{n}}} + \frac{K_s}{A} \left((\hat{\mathbf{n}} \cdot \mathbf{m}) \hat{\mathbf{n}} \times \hat{\mathbf{x}}_M + (\hat{\mathbf{n}} \cdot \hat{\mathbf{x}}_M) \hat{\mathbf{n}} \times \mathbf{m} \right) = 0, \quad (2)$$

where $\hat{\mathbf{n}}$ is surface normal. For $\hat{\mathbf{x}}_M = \hat{\mathbf{x}}$ and $\hat{\mathbf{n}} = \hat{\mathbf{y}}$ [Fig. 2(a)], expression (2) simplifies to:

$$\begin{aligned} \frac{\partial m_y}{\partial n} - \frac{K_s}{A} m_y &= 0, \\ \frac{\partial m_z}{\partial n} &= 0. \end{aligned} \quad (3)$$

It is worth noting that the surface anisotropy constant K_s is the only spatially dependent parameter in the system. Therefore,

the patterning of the Bragg mirrors for spin waves is achieved by spatially varying the boundary conditions, due to the $K_s(x)$ dependence.

The linearized form of Eq. 1 takes the form:

$$\begin{aligned} -i\omega m_y + \frac{2A\gamma}{M_s} \Delta m_z - \frac{2A\gamma}{M_s} k_z^2 m_z - \gamma\mu_0 H_0 m_z - iM_s \gamma\mu_0 k_z \varphi &= 0, \\ -i\omega m_z - \frac{2A\gamma}{M_s} \Delta m_y + \frac{2A\gamma}{M_s} k_z^2 m_y + \gamma\mu_0 H_0 m_y + M_s \gamma\mu_0 \frac{\partial \varphi}{\partial y} &= 0 \end{aligned} \quad (4)$$

along with the Gauss equation for magnetism inside ferromagnet ($\mathbf{m} \neq 0$) and outside ferromagnet ($\mathbf{m} = 0$):

$$\frac{\partial^2 \varphi}{\partial x^2} + \frac{\partial^2 \varphi}{\partial y^2} - k_z^2 \varphi - \frac{\partial m_y}{\partial y} - ik_z m_z = 0. \quad (5)$$

For uniformity in z -direction, solutions take plane wave form $e^{ik_z z}$ with amplitudes $m_y(x, y)$, $m_z(x, y)$, $\varphi(x, y)$. Eqs. 4, 5 together with boundary conditions (2) were implemented in the mathematical module of the COMSOL Multiphysics³³ and solved via finite element method for:

- (i) *Unit cell of infinite magnonic crystal* – determining frequency gaps: Bloch boundary conditions in x -direction for 2D wave vector $\mathbf{k} = k_x \hat{\mathbf{x}} + k_z \hat{\mathbf{z}}$ were applied to find gap edges of magnonic crystal for given value of k_z .
- (ii) *Full waveguide structure* – determining the 1D dispersion of waveguide modes: periodic boundary conditions were applied at both ends of the whole structure (two 21-period Bragg mirrors) to enable the study of weakly localized waveguide modes.

Both systems include non-magnetic regions ($1000 \times$ thickness) above and below considered structure to correctly calculate dynamic demagnetizing field effects.

We investigated the structure shown in Fig. 2(a): a 6-nm-thick $\text{Co}_{20}\text{Fe}_{60}\text{B}_{20}$ layer with low spin-wave damping ($\alpha = 0.0029$)³⁶. Surface anisotropy was applied at both $\text{Co}_{20}\text{Fe}_{60}\text{B}_{20}$ interfaces. The regions with surface anisotropy (red strips) are arranged periodically, forming Bragg mirrors that confine spin waves in a wider central strip. The structure thus acts as a defected magnonic crystal with a 100-nm period (50-nm anisotropy strips alternating with 50-nm wide sections of pristine $\text{Co}_{20}\text{Fe}_{60}\text{B}_{20}$ layer) and a defect region defined by a single 150-nm-wide anisotropy strip. Volume magnetocrystalline anisotropy was neglected.

We used experimental values: saturation magnetization $M_s = 1150 \text{ kA/m}$ ³⁷, exchange stiffness $A = 28 \text{ pJ/m}$ ³⁶, and gyromagnetic ratio $|\gamma| = 176 \text{ rad/T/ns}$ ³⁶. We assumed a surface anisotropy $K_s = 1.05 \text{ mJ/m}^2$ at both interfaces, corresponding to an effective volume anisotropy $K_v = 2K_s/t$ for CoFeB/MgO with a Ta cap³⁷; see the inset in Fig. 2(a). Experiments³⁷ do not separate the CoFeB/MgO and CoFeB/Ta contributions, but for a thin ferromagnetic layer this is not critical: Supplementary Material 1 shows that using $K_s = 2.1 \text{ mJ/m}^2$ at a single interface yields a dispersion almost identical to that in Fig. 2(b). Since the CoFeB/MgO interfacial anisotropy nearly vanishes for ultrathin MgO ³⁸, a structure can be fabricated by modulating the MgO thickness. The structure can be manufactured by (i) patterning trenches in SiO_2 , (ii) sputtering

MgO (< 0.5 nm on ridges, 1 nm in trenches), (iii) depositing a 6 nm CoFeB layer and Ta cap, and (iv) selectively removing Ta above the SiO₂ ridges using focused ion-beam milling.

An external field ($\mu_0 H_0 = 500$ mT) was applied in the x -direction, perpendicular to the stripes and tangential to the film. In this Damon-Eshbach geometry, spin waves propagate perpendicular to the field, resulting in high group velocity. Unlike the ferromagnetic strip [Fig. 1(a)], this structure avoids edge modes due to the absence of static demagnetization.

The choice of a 6 nm thickness represents a balance between high group velocity, which increases with t , and strong effective anisotropy, which decreases with t (see Supplementary Material 2). A large anisotropy contrast allows for wide frequency gaps and strong confinement, while a 50% filling fraction further enhances the gap width. The 100 nm lattice constant provides a broad first Brillouin zone, giving access to multiple low-frequency bands at comparatively high frequencies.

Due to magnetic anisotropy, the ferromagnetic resonance (FMR) frequency in a ferromagnetic layer is non-zero for non-zero applied field. Above the FMR frequency, the wave vector becomes real, enabling spin waves to propagate. Below the FMR frequency, it becomes complex, resulting in unphysical exponential changes in spin-wave amplitude. This can be exploited to build a waveguide (see Fig. 1(c)). By tuning material parameters in the waveguide region, spin-wave profiles become oscillatory inside and decay exponentially in the surrounding layer, but only for frequencies up to the FMR. This limit is lifted using a pair of magnonic crystals as Bragg mirrors. The system (see Fig. 2(a)) overcomes this constraint and enables waveguiding at higher frequencies, within frequency gaps where complex wave vectors ensure confinement.

This feature is clearly visible in Fig. 2(b), where the waveguide modes (solid lines) appear in several frequency gaps (white regions), including those located well above the FMR frequency of the uniform layer (dotted black line). These modes propagate along the waveguide with the real wave number k_z and decaying when penetrating the Bragg mirrors at the exponential rate given by the imaginary part of the wave vector k_x from the frequency gap of the magnonic crystals (Bragg mirrors). Within the considered frequency range (20–45 GHz), one or two waveguide modes can be observed in each successive frequency gap. However, the number of these modes can increase in each gap if a wider waveguide is considered. The number of waveguide modes in a given gap also depends on the width of the gap, which, in turn, is determined by the parameters of the Bragg mirrors.

Let us discuss in more detail the advantages of the proposed design. The large group velocity and strong localization are essential features of the waveguide that determine its performance. Only a sufficiently high value of the group velocity allows for the transmission of spin-wave signals over practical distances in the presence of damping. On the other hand, strong localization within the waveguide reduces cross-talk between different waveguides in the system.

Fig. 3 shows the group velocity of the waveguide modes, $v_g = d\omega/dk_z$, calculated from the dispersion relation. The

group velocity of all modes increases with the wave vector k_z . For smaller values of k_z , the waveguide modes with the lowest frequencies (brownish and reddish lines) exhibit higher group velocities; however, for larger k_z , this order is reversed. The obtained values of group velocity are suitable for spin-wave transmission in low-damping materials such as CoFeB. However, the transmission of spin waves with long wavelengths is inefficient, as v_g approaches zero for $k_z \rightarrow 0$. Knowing the group velocity, we can calculate the spin-wave decay length L_d in the presence of Gilbert damping, as discussed in Supplementary Material, Section 3, where we show that for CoFeB, L_d defined by $m_y(z + L_d)/m_y(z) = 1/e$ is significantly larger

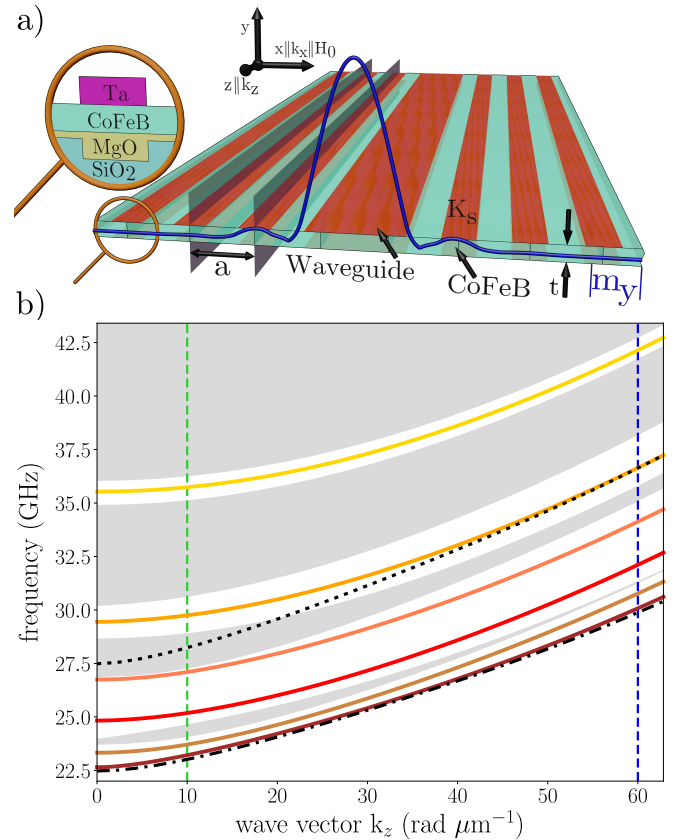


FIG. 2. (a) Structure under study: spin waves are confined by two Bragg mirrors (red stripes) formed by periodically modulated surface anisotropy on the top and bottom surfaces. Waves are guided along z in the central region (wider strip – defect). The anisotropy is set by K_s and the mirror period by a . The static field H_0 is applied in-plane, perpendicular to the waveguide. The blue line shows an exemplary out-of-plane profile $|m_y|$. The inset illustrates a possible experimental realization. (b) Dispersion $f(k_z)$ of the waveguide modes (colored lines). Modes are confined when their frequencies fall into the band gaps of the magnonic crystals (white regions). The lower limit is the FMR of a uniform layer with continuous surface anisotropy on both sides (dash-dotted black line); for this design, higher-order modes (e.g., Nos. 5–6) can appear even above the FMR of a uniform layer without surface anisotropy (dotted line). Vertical dashed lines indicate the k_z values used for mode profiles in Fig. 5; for $k_z = 10$ rad/μm we also evaluate a figure of merit for the trade-off between propagation and localization (see Supplementary Material 2).

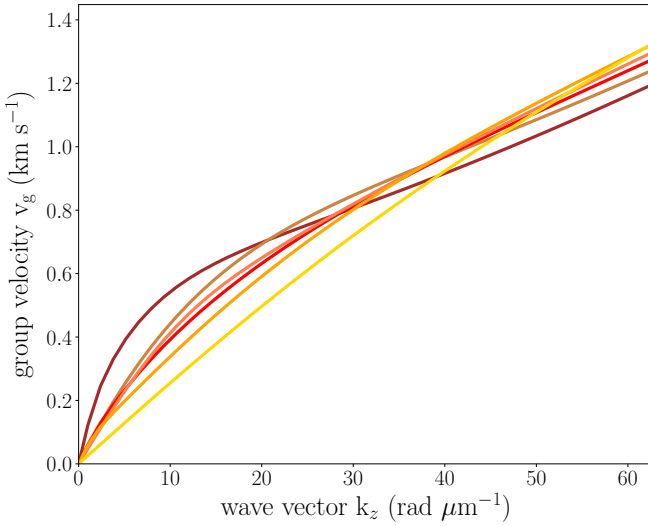


FIG. 3. Group velocity of the waveguide modes as a function of the wave vector $v_g(k_z)$. Line colors denote successive modes with increasing frequencies (see Fig. 2(b)).

than a few waveguide (defect) widths.

The localization of waveguide modes is primarily determined by the complex wave vector, k_x , within the frequency gaps of the magnonic crystals. It is well established³⁹ that the imaginary part of the wave vector reaches its maximum within the frequency gap, indicating the strongest localization, and decreases toward the band edges. However, we used a general measure of localization: the Inverse Participation Ratio (IPR), which can be calculated from the profile of waveguide modes, $|m_y|$, across the entire structure. We computed a discrete approximation of the IPR⁴⁰:

$$\widetilde{\text{IPR}} = \text{IPR} \frac{S}{mn} = \frac{\sum_{i,j}^{m,n} |m_y(x_i, y_j)|^4}{\left(\sum_{i,j}^{m,n} |m_y(x_i, y_j)|^2\right)^2}, \quad (6)$$

with $S = 43at$ - cross-section area of the ferromagnetic layer, $n = 36$ - points across the thickness, $m = 4300$ - points along the layer. $\widetilde{\text{IPR}}$ ranges from $1/(mn)$ (uniform distribution) to 1 (point localization).

Fig. 4 shows the dependence of $\widetilde{\text{IPR}}$ on the wave vector k_z for successive waveguide modes. The values are highest for modes 1–3 (brownish and reddish lines), as reflected in the mode profiles in Fig. 5. These modes have frequencies below the FMR frequency of the uniform ferromagnetic layer, meaning the spin wave must tunnel through regions of the Bragg mirror without surface anisotropy. This results in faster spatial decay across the mirrors: $\pm e^{\mp \text{Im}(k_x)x}$. Such decay corresponds to wider frequency gaps, where $\text{Im}(k_x)$ is larger.

Higher-frequency modes (e.g., Nos. 4–6 – yellowish and pink lines) can only be localized by Bragg mirrors. For modes like No. 4 and No. 5, localization strength varies with k_z . This is seen in the frequency shifts of these modes in Fig. 2(b). As k_z increases, mode No. 4 moves away from the gap edge, while No. 5 approaches it. Both a mode's proximity to the gap

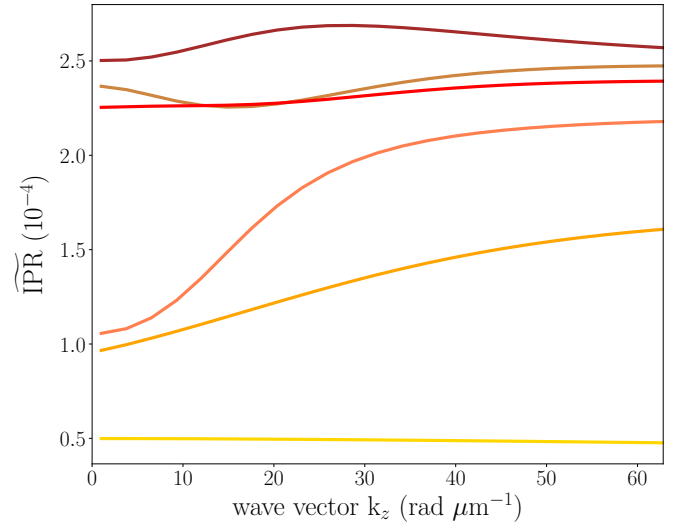


FIG. 4. Measure of the localization of the waveguide modes: modified inverse participation ratio as a function of the wave vector $\widetilde{\text{IPR}}(k_z)$ – see Eq.6. Line colors denote successive modes with increasing frequencies (see Fig. 2(b)).

center and the gap's width are known³⁹ to enhance localization in periodic structures via increased $\text{Im}(k_x)$. These effects are visible in the profiles of modes No. 4 and No. 5 in Fig. 5 (green and blue lines correspond to different k_z values).

Notably, $\widetilde{\text{IPR}}$ and v_g are interdependent. Increasing the ferromagnetic layer thickness t boosts v_g ⁴¹, but reduces the effective anisotropy $K_{\text{eff}} = -\mu_0 M_s^2 + K_s/t$, weakening the spatial modulation. This reduces the Bragg mirror effect, narrows the frequency gaps, and lowers localization strength (as measured by $\widetilde{\text{IPR}}$). We discuss the optimal layer thickness and the balance between v_g and $\widetilde{\text{IPR}}$ in Supplemental Material 2.

The system is a multimode waveguide where successive modes differ in the number of nodes [Fig. 2(b)]. Mode profiles (blue and green lines in Fig. 5) reveal two distinct regions: the defect (wider red strip in Fig. 5) with nearly constant amplitude, and the Bragg mirrors with exponentially decaying amplitude. The number of nodes increases from 0 to 4 (for modes 1–5) with frequency, regardless of whether the modes appear singly or in pairs within the gaps [Fig. 2(b)]. The IPR is related to the distance ensuring isolation between two waveguides, L_i , which can be determined from the SW profile using the condition $10 \log_{10}(|m_y(L_i)|^2 / |m_{y,0}|^2) = -20$ dB, where $|m_{y,0}|$ is the maximum dynamic magnetization inside the waveguide. For $k = 10 \text{ rad}/\mu\text{m}$ (green lines in Fig. 5), this yields $L_i = 0.40, 1.68, 2.66$, and 6.23 defect widths for modes 3–6; for the more focused modes 1 and 2, L_i is even smaller but difficult to extract reliably from $m_y(x)$.

The proposed design offers several advantages: it uses a homogeneously magnetized, low-damping ferromagnetic film and requires only periodic patterning of a nonmagnetic over(under)layer to form anisotropy-induced Bragg mirrors, suppressing static demagnetizing fields and eliminating edge modes typical of strip waveguides. Bragg confinement also enables guiding of spin waves at frequencies above the ferro-

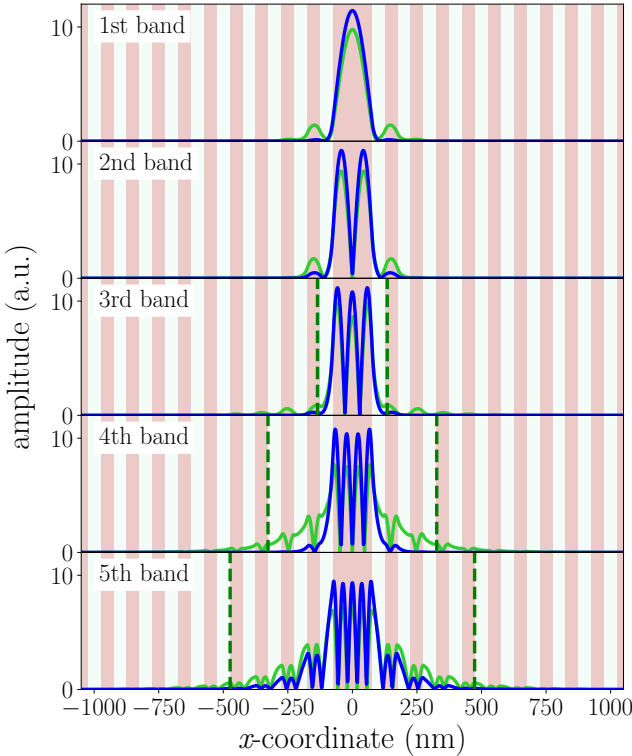


FIG. 5. Profiles of the out-of-plane component of the dynamic magnetization, $|m_y|$, for successive waveguide modes at two selected wave vectors: $k_z = 10 \text{ rad}/\mu\text{m}$ (green) and $k_z = 60 \text{ rad}/\mu\text{m}$ (blue). See Fig. 2(b) for the corresponding dispersion branches. Pink (white) regions indicate sections of the ferromagnetic layer with (without) surface anisotropy. Green dashed lines indicate the isolation distance L_i necessary to prevent crosstalk between adjacent waveguides in integrated circuits.

magnetic resonance of a uniform layer, which simpler designs cannot achieve. This, however, involves a trade-off between high group velocity and strong confinement, requiring relatively thin ferromagnetic layers and sufficiently large surface anisotropy.

SUPPLEMENTARY MATERIAL

The supplementary material is divided into three sections. The first section presents the dispersion relation for a doubled surface anisotropy constant applied at a single surface (e.g., the top surface only), as well as the dispersion relation obtained using realistic values for voltage-controlled magnetic anisotropy. The second section provides the figure of merit calculated for our structure. The third section describes the methodology for calculating the decay length and presents its dependence on the wave vector.

ACKNOWLEDGMENTS

This work has received funding from National Science Centre Poland grants UMO-2020/39/O/ST5/02110, UMO-2021/43/I/ST3/00550, and support from the Polish Science National Agency for Academic Exchange grant BPN/PRE/2022/1/00014/U/00001.

DATA AVAILABILITY STATEMENT

The data for the essential figures (Fig. 2(b), Fig. 3, Fig. 4) can be accessed via the following <https://doi.org/10.5281/zenodo.14580873>. The remaining data is available from the corresponding author on reasonable request.

CONFLICT OF INTEREST STATEMENT

The authors have no conflicts to disclose.

AUTHOR CONTRIBUTIONS STATEMENT

G. C.: Data curation, Formal analysis, Funding acquisition, Investigation, Methodology, Software, Validation, Visualization, Writing – original draft, Writing – review and editing.
J. W. K.: Conceptualization, Data curation, Formal analysis, Funding acquisition, Investigation, Methodology, Project administration, Resources, Software, Supervision, Validation, Visualization, Writing – original draft, Writing – review and editing.

REFERENCES

- Q. Wang, A. V. Chumak, and P. Pirro, “Inverse-design magnonic devices,” *Nat. Comm.* **12**, 2636 (2021).
- Y. Li, W. Zhang, V. Tyberkevych, W.-K. Kwok, A. Hoffmann, and V. Novosad, “Hybrid magnonics: Physics, circuits, and applications for coherent information processing,” *J. Appl. Phys.* **128**, 130902 (2020).
- Q. Wang, G. Csaba, R. Verba, A. V. Chumak, and P. Pirro, “Nanoscale magnonic networks,” *Phys. Rev. Appl.* **21**, 040503 (2024).
- X. Han, H. Wu, and T. Zhang, “Magnonics: Materials, physics, and devices,” *Appl. Phys. Lett.* **125**, 020501 (2024).
- A. Khitun and K. L. Wang, “Nano scale computational architectures with spin wave bus,” *Superlattice. Microst.* **38**, 184–200 (2005).
- L. Zheng, L. Jin, T. Wen, Y. Liao, X. Tang, H. Zhang, and Z. Zhong, “Spin wave propagation in uniform waveguide: effects, modulation and its application,” *J. Phys. D: Appl. Phys.* **55**, 263002 (2022).
- M. P. Kostylev, G. Gubbiotti, J.-G. Hu, G. Carlotti, T. Ono, and R. L. Stamps, “Dipole-exchange propagating spin-wave modes in metallic ferromagnetic stripes,” *Phys. Rev. B* **76**, 054422 (2007).
- V. E. Demidov, S. O. Demokritov, K. Rott, P. Krzysteczko, and G. Reiss, “Mode interference and periodic self-focusing of spin waves in permalloy microstripes,” *Phys. Rev. B* **77**, 064406 (2008).
- P. Pirro, T. Brächer, K. Vogt, B. Obry, H. Schultheiss, B. Leven, and B. Hillebrands, “Interference of coherent spin waves in micron-sized ferromagnetic waveguides,” *phys. status solidi (b)* **248**, 2404–2408 (2011).

¹⁰G. Duerr, K. Thurner, J. Topp, R. Huber, and D. Grundler, “Enhanced transmission through squeezed modes in a self-cladding magnonic waveguide,” *Phys. Rev. Lett.* **108**, 227202 (2012).

¹¹X. Xing, S. Li, X. Huang, and Z. Wang, “Engineering spin-wave channels in submicrometer magnonic waveguides,” *AIP Adv.* **3**, 032144 (2013).

¹²B. Obry, P. Pirro, T. Brächer, A. V. Chumak, J. Osten, F. Ciubotaru, A. A. Serga, J. Fassbender, and B. Hillebrands, “A micro-structured ion-implanted magnonic crystal,” *Appl. Phys. Lett.* **102**, 202403 (2013).

¹³J. Ding and A. O. Adeyeye, “Binary ferromagnetic nanostructures: Fabrication, static and dynamic properties,” *Adv. Funct. Mater.* **23**, 1684–1691 (2013).

¹⁴G. Centała, M. L. Sokolovskyy, C. S. Davies, M. Mruczkiewicz, S. Mamica, J. Rychly, J. W. Kłos, V. V. Kruglyak, and M. Krawczyk, “Influence of non-magnetic dielectric spacers on the spin-wave response of one-dimensional planar magnonic crystals,” *Phys. Rev. B* **100**, 224428 (2019).

¹⁵E. Albisetti, D. Petti, M. Pancaldi, M. Madami, S. Tacchi, J. Curtis, W. P. King, A. Papp, G. Csaba, W. Porod, P. Vavassori, E. Riedo, and R. Bertacco, “Nanopatterning reconfigurable magnetic landscapes via thermally assisted scanning probe lithography,” *Nat. Nanotechnol.* **11**, 545–551 (2016).

¹⁶S. J. Hämäläinen, M. Madami, H. Qin, G. Gubbiotti, and S. van Dijken, “Control of spin-wave transmission by a programmable domain wall,” *Nat. Commun.* **9**, 4853 (2018).

¹⁷L. Wang, L. Gao, L. Jin, Y. Liao, T. Wen, X. Tang, H. Zhang, and Z. Zhong, “Magnonic waveguide based on exchange-spring magnetic structure,” *AIP Adv.* **8**, 055103 (2018).

¹⁸F. Garcia-Sanchez, P. Borys, R. Soucaille, J.-P. Adam, R. L. Stamps, and J.-V. Kim, “Narrow magnonic waveguides based on domain walls,” *Phys. Rev. Lett.* **114**, 247206 (2015).

¹⁹K. Wagner, A. Käkay, K. Schultheiss, A. Henschke, T. Sebastian, and H. Schultheiss, “Magnetic domain walls as reconfigurable spin-wave nanochannels,” *Nat. Nanotechnol.* **11**, 432–436 (2016).

²⁰M. Vogel, A. V. Chumak, E. H. Waller, T. Langner, V. I. Vasyuchka, B. Hillebrands, and G. Von Freymann, “Optically reconfigurable magnetic materials,” *Nat. Phys.* **11**, 487–491 (2015).

²¹A. D. Karenowska, J. F. Gregg, V. S. Tiberkevich, A. N. Slavin, A. V. Chumak, A. A. Serga, and B. Hillebrands, “Oscillatory energy exchange between waves coupled by a dynamic artificial crystal,” *Phys. Rev. Lett.* **108**, 015505 (2012).

²²M. Langer, F. Röder, R. A. Gallardo, T. Schneider, S. Stienen, C. Gatel, R. Hübner, L. Bischoff, K. Lenz, J. Lindner, P. Landeros, and J. Fassbender, “Role of internal demagnetizing field for the dynamics of a surface-modulated magnonic crystal,” *Phys. Rev. B* **95**, 184405 (2017).

²³B. Rana and Y. Otani, “Voltage-controlled reconfigurable spin-wave nanochannels and logic devices,” *Phys. Rev. Appl.* **9**, 014033 (2018).

²⁴X. Li, K. Fitzell, D. Wu, C. T. Karaba, A. Buditama, G. Yu, K. L. Wong, N. Altieri, C. Grezes, N. Kioussis, S. Tolbert, Z. Zhang, J. P. Chang, P. Khalili Amiri, and K. L. Wang, “Enhancement of voltage-controlled magnetic anisotropy through precise control of Mg insertion thickness at CoFeB|MgO interface,” *Appl. Phys. Lett.* **110**, 052401 (2017).

²⁵S. Choudhury, A. K. Chaurasiya, A. K. Mondal, B. Rana, K. Miura, H. Takahashi, Y. Otani, and A. Barman, “Voltage controlled on-demand magnonic nanochannels,” *Sci. Adv.* **6**, eaba5457 (2020).

²⁶Q. Wang, A. V. Chumak, L. Jin, H. Zhang, B. Hillebrands, and Z. Zhong, “Voltage-controlled nanoscale reconfigurable magnonic crystal,” *Phys. Rev. B* **95**, 134433 (2017).

²⁷J. W. Kłos, Y. S. Dadoenkova, J. Rychły, N. N. Dadoenkova, I. L. Lyubchanskii, and J. Barnas, “Hartman effect for spin waves in exchange regime,” *Sci. Rep.* **8**, 17944 (2018).

²⁸J. Zhao, L. Feng, M. Ma, and F. Ma, “Three-terminal magnonic demultiplexer, power divider, and circulator,” *J. Magn. Magn. Mater.* **586**, 171161 (2023).

²⁹M. A. Morozova, A. V. Sadovnikov, O. V. Matveev, A. Y. Sharaevskaya, Y. P. Sharaevskii, and S. A. Nikitov, “Band structure formation in magnonic bragg gratings superlattice,” *J. Phys. D: Appl. Phys.* **53**, 395002 (2020).

³⁰R. A. Gallardo, T. Schneider, A. Roldán-Molina, M. Langer, A. S. Núñez, K. Lenz, J. Lindner, and P. Landeros, “Symmetry and localization properties of defect modes in magnonic superlattices,” *Phys. Rev. B* **97**, 174404 (2018).

³¹J. W. Kłos and V. S. Tkachenko, “Symmetry-related criteria for the occurrence of defect states in magnonic superlattices,” *J. Appl. Phys.* **113**, 133907 (2013).

³²A. Gurevich and G. Melkov, *Magnetization Oscillations and Waves* (Taylor & Francis, 1996).

³³K. Szulc, S. Tacchi, A. Hierro-Rodríguez, J. Díaz, P. Gruszecki, P. Graczyk, C. Quirós, D. Markó, J. I. Martín, M. Vélez, D. S. Schmool, G. Carlotti, M. Krawczyk, and L. M. Álvarez Prado, “Reconfigurable magnonic crystals based on imprinted magnetization textures in hard and soft dipolar-coupled bilayers,” *ACS Nano* **16**, 14168–14177 (2022), PMID: 36043881.

³⁴G. Centała and J. W. Kłos, “Shaping magnetization dynamics in a planar square dot by adjusting its surface anisotropy,” *J. Magn. Magn. Mater.* **587**, 171254 (2023).

³⁵COMSOL Inc., “COMSOL Multiphysics,” Stockholm, Sweden.

³⁶H. Wang, W. He, R. Yuan, Y. Wang, J. Wang, Y. Zhang, I. Medlej, J. Chen, G. Yu, X. Han, J.-P. Ansermet, and H. Yu, “Hybridized propagating spin waves in a CoFeB/IrMn bilayer,” *Phys. Rev. B* **106**, 064410 (2022).

³⁷D.-S. Lee, H.-T. Chang, C.-W. Cheng, and G. Chern, “Perpendicular magnetic anisotropy in MgO/CoFeB/Nb and a comparison of the cap layer effect,” *IEEE Trans. Magn.* **50**, 1–4 (2014).

³⁸M. Yamanouchi, R. Koizumi, S. Ikeda, H. Sato, K. Mizunuma, K. Miura, H. D. Gan, F. Matsukura, and H. Ohno, “Dependence of magnetic anisotropy on mgo thickness and buffer layer in co20fe60b20-mgo structure,” *J. Appl. Phys.* **109**, 07C712 (2011).

³⁹W. Kohn, “Analytic properties of bloch waves and wannier functions,” *Phys. Rev.* **115**, 809–821 (1959).

⁴⁰D. Thouless, “Electrons in disordered systems and the theory of localization,” *Phys. Rep.* **13**, 93–142 (1974).

⁴¹D. Stancil and A. Prabhakar, *Spin Waves: Theory and Applications* (Springer US, 2009).